Bio-Design and Manufacturing (2023) 6:268–283
https://doi.org/10.1007/s42242-022-00223-1

RESEARCH ARTICLE

Development of a portable reflectance confocal microscope and its application in the noninvasive in vivo evaluation of mesenchymal stem cell-promoted cutaneous wound healing

Lixing Zhang[1,3] · Xin Miao[1,4] · Meijia Wang[1] · Aihua Shi[1] · Jingwen Wang[1] · Zhonglin Ma[5] · Yunhai Zhang[1] · Jingzhong Zhang[1,2,3] · Shuang Yu[1,2,3]

Received: 23 June 2022 / Accepted: 15 November 2022 / Published online: 12 December 2022

Abstract

The process of wound healing is routinely evaluated by histological evaluation in the clinic, which may cause scarring and secondary injury. Reflectance confocal microscopy (RCM) represents a noninvasive, real-time imaging technique that allows in vivo evaluation of the skin. Traditional RCM was wide-probe-based, which limited its application on uneven and covered skin. In this study, we report the development of a portable reflectance confocal microscope (PRCM) in which all components were assembled in a handheld shell. Although the size and weight of the PRCM were reduced based on the use of a microelectromechanical system, the resolution was kept at 0.91 μm, and the field of view of the system was 343 μm × 532 μm. When used in vivo, the PRCM was able to visualize cellular and nuclear morphology for both mouse and human skin. PRCM evaluations were then performed on wounds after topically applied mesenchymal stem cells (MSCs) or saline treatment. The PRCM allowed visualization of the formation of collagen bundles, re-epithelization from the wound edge to the wound bed, and hair follicle regeneration, which were consistent with histological evaluations. Therefore, we offer new insights into monitoring the effects of topically applied MSCs on the process of wound healing by using PRCM. This study illustrates that the newly developed PRCM represents a promising device for real-time, noninvasive monitoring of the dynamic process of wound healing, which demonstrates its potential to diagnose, monitor, or predict disease in clinical wound therapy.

Lixing Zhang and Xin Miao have contributed equally to this work.

✉ Jingzhong Zhang
zhangjz@sibet.ac.cn

✉ Shuang Yu
yush@sibet.ac.cn

1 Suzhou Institute of Biomedical Engineering and Technology (SIBET), Chinese Academy of Sciences, Suzhou 215163, China

2 Department of Biomedical Engineering, School of Medical Imaging, Xuzhou Medical University, Xuzhou 221004, China

3 Zhengzhou Zhongke Institute of Biomedical Engineering and Technology Affiliated with SIBET, Zhengzhou 450001, China

4 School of Biomedical Engineering (Suzhou), Division of Life Sciences and Medicine, University of Science and Technology of China, Hefei 230026, China

5 School of Radiation Medicine and Protection, Soochow University, Suzhou 215123, China

Graphic abstract

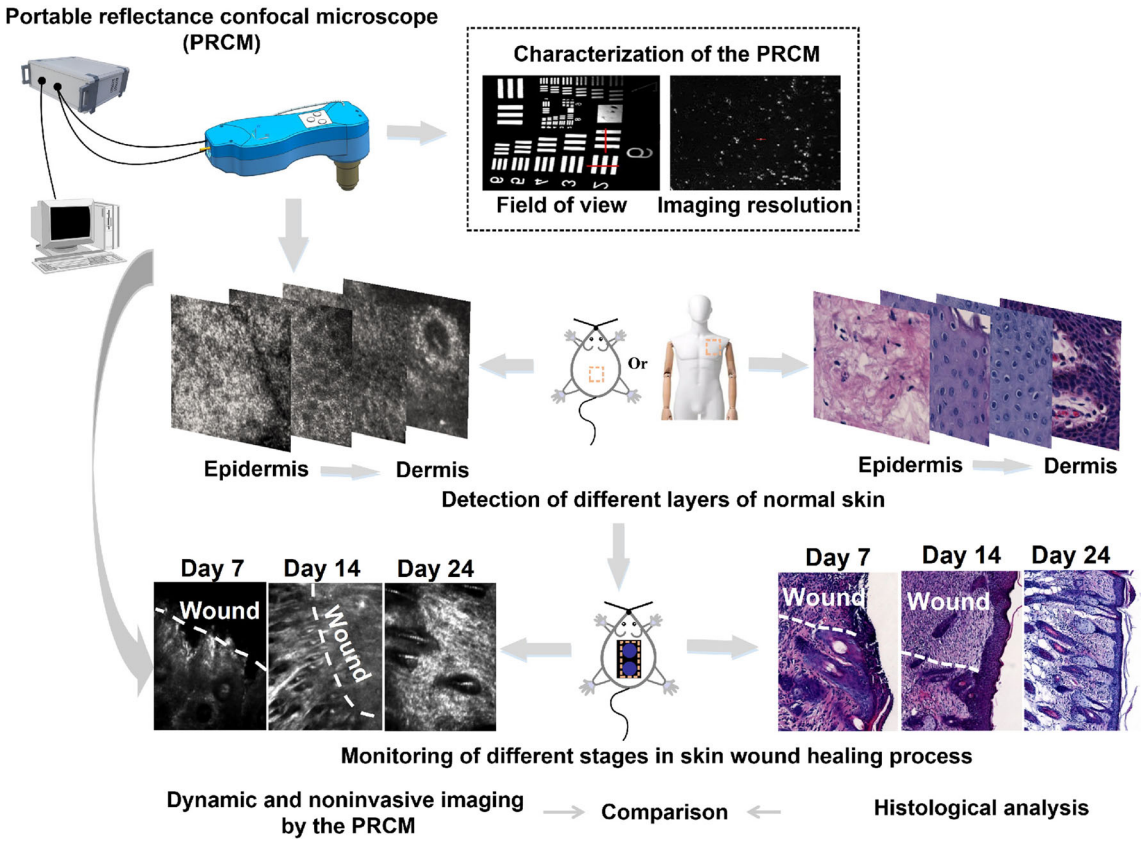

Keywords Portable reflectance confocal microscope · Wound healing · Noninvasive optical imaging · Real-time in vivo visualization

Introduction

Skin is the most superficial organ of the body, and damage to skin will cause fluid loss, microbial infection, and other problems. Effective diagnosis and monitoring of such wounds can lead to better treatments, quicker healing, and significant reduction in health care costs [1, 2].

In the clinic, visual observation is commonly used for preliminary diagnosis and monitoring of skin wounds [3]. Overall wound morphology and aspects of wound healing progress can be assessed. However, visual observation is not able to observe the re-epithelization and regeneration of fibroblasts and collagen fibers during wound healing, which is important for developing better and effective wound treatments [4]. Serial histological evaluation was also performed to monitor wound repair. However, biopsies may cause scar formation and the risk of infection. Furthermore, sequential biopsies may impair the process of wound healing, and evaluations of the same area over time can have significant adverse effects on wound healing. Currently, noninvasive imaging techniques are used for a preliminary diagnosis of skin pathology, such as optical coherence tomography [5], digital dermoscopy [6], and reflectance confocal microscopy (RCM) [7]. Digital dermoscopy has been widely used for surface imaging of the skin in the past few years. Although the cost is low, the limited resolution impedes its further application in precision diagnosis at the cellular level. Optical coherence tomography (OCT) is a longitudinal imaging method with a resolution of 2–10 μm; however, difficulty in OCT data processing hampers its promotion in the clinic. One of the most promising techniques for assessing skin pathology is RCM, which is an optical imaging technique. RCM uses a laser diode as a source of coherent monochromatic light, and the illumination and detection optics are focused on the same diffraction-limited spot. Complete images can be built on the detector when the optics are moved over the sample. Optical sectioning is provided during scanning. The entire field of view is illuminated during confocal imaging, and anything outside the focal plane contributes little to the image [8]. Different contrasts in the refractive index of the

cell organelles and microstructures result in capturing images with white structures on a black background. RCM imaging performed parallel to the skin surface can complement pathological examination [9]. Moreover, RCM can offer a dynamic and repeated noninvasive analysis of skin tissue.

It has been reported that RCM allowed for the noninvasive evaluation of pigmentary disorders based on melanin content [10] and was applied to conditions such as hypopigmentary disorders and pigmented skin tumors [11]. RCM can also be used to assess the epidermis and vesicle formation when inflammatory skin diseases are diagnosed, such as contact dermatitis and folliculitis [12]. Epidermal thickness and melanocytes in guinea pigs were also detected by RCM [13]. Furthermore, RCM has been shown to significantly improve the detection of inflammatory cells, collagen structure, and blood vessels after allotransplantation in rats and human patients [14, 15].

Although RCM has been approved by the US Food and Drug Administration as an optical imaging technology that offers noninvasive visualization of skin lesions in vivo, the current commercially available in vivo devices only include VivaScope 1500 (Caliber ID, Rochester, NY, USA) and VivaScope 3000 (Caliber ID, Rochester, NY, USA) [16]. VivaScope 1500 is a traditional wide-probe-based RCM and requires attaching a metal ring onto the skin, which poses a challenge for narrow, covered and uneven skin. Conversely, the handheld VivaScope 3000 allows free-form translation on the skin along any user-chosen path, permitting its use on concave or curved areas such as the nose, ears, and eyes [17]. However, the high cost of purchasing a handheld RCM device limits its use to large academic and clinical centers.

Mesenchymal stem cells (MSCs) can be obtained from bone marrow, adipose tissue, and the umbilical cord [18]. Transplantation of MSCs to skin wounds has been demonstrated to impair wound healing. MSCs coordinate the inflammatory process, modulate fibrosis, and reduce scarring with the advantages of strong immunomodulatory characteristics and the effect of releasing growth factors [19, 20]. Whether the RCM could be used for monitoring dynamic changes after application of MSCs to the wounded skin needs further investigation.

In this study, we developed an RCM device using a microelectromechanical system (MEMS) instead of the traditional mechanical scanning galvanometer. The use of MEMS reduced the weight and size of the RCM and made it portable. Moreover, the resolution of the device was 0.91 μm, and the imaging speed was 8 frames/s, which were comparable to the commercial RCM. When used in vivo, portable reflectance confocal microscope (PRCM) imaging provided the cellular and nuclear morphology of both mouse and human skin. To evaluate the use of PRCM for monitoring dynamic changes in skin wound repair, spontaneous and MSC-promoted wound healing was evaluated using PRCM and histological staining at multiple time points. The results of our study showed that dynamic changes during wound healing, including collagen formation, re-epithelization, and hair follicle regeneration, could be well captured by the PRCM, and these events were consistent with pathological detection. The newly developed PRCM showed the potential to act as a noninvasive and real-time tool for monitoring the wound healing process both longitudinally and at various sites.

Materials and methods

PRCM design and setup

Here, we developed PRCM consisting of a scanning head, electric control panel and master computer, as shown in Figs. 1a and 1b. The scanning head was the key component of the PRCM and was composed of an illumination module, beam expander module, detection module, scanning module and imaging module (Fig. 2a). In detail, the illumination module consisted of a single-mode polarization-maintaining fiber (Thorlabs, P1-780PM-FC-1, USA), laser (Pavilion Integration Crop., W830-50FC-204, China) and a polarized beam splitter (PBS, Thorlabs, PBS052, USA). The beam expander module consisted of a scanning lens and field mirrors. The detection module (Fig. S1 in Supplementary Information) consisted of a pinhole lens and multimode fibers (Thorlabs, M67L01, USA). The scanning module consisted of a MEMS and mirrors. MEMS, the key element of the scanning module, plays a critical role in driving beam scanning. The diameter of the MEMS scanning galvanometer is 3 mm. The mechanical scanning angle of the fast axis is ±5° (tolerance is ±1°), while the mechanical scanning angle of the slow axis is ±3° (tolerance is ±1°). The fast axis scanning frequency is 12 kHz. The imaging module consisted of a quarter wave plate and objective lens (Olympus, LUMPLFLN40XW, Japan).

The electric control panel provided power for the hardware of the PRCM and carried out automatic control of the system. It was internally integrated with the main control board, switching power (MEAN WELL, RS-50-12, China), light source control box, detection circuit board, step-down module (JXINW, LM2596, China), etc.

The master computer played the role of sending commands and state feedback to PRCM, which acted as the upper monitor system. A high-speed data acquisition board (NI, PCI5105, USA) was integrated into the master computer. The upper monitor consisted of a light source control module, motion control module, image acquisition module, image saving module, atlas comparison module, database input module and image display window.

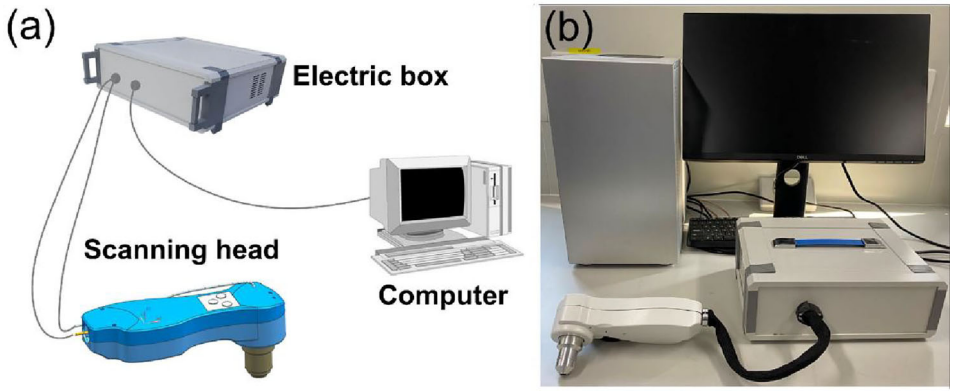

Fig. 1 Systematic composition of a portable reflectance confocal microscope (PRCM). **a** Schematic of the control relationship between the internal components of the PRCM. **b** The exterior components of the PRCM

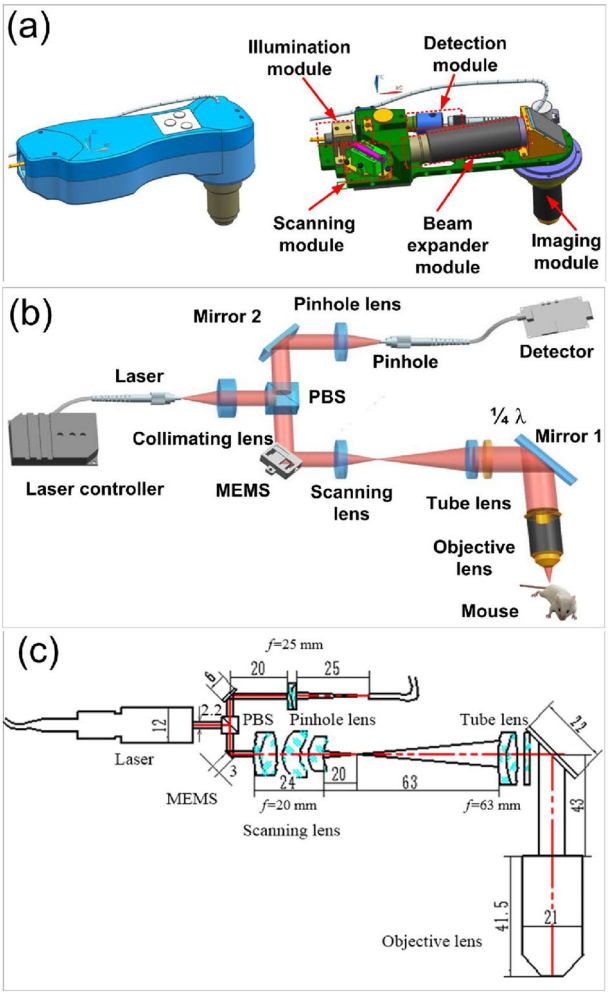

Fig. 2 Internal structure and optical system of the scanning head from the portable reflectance confocal microscope (PRCM). **a** Module composition of the scanning head. **b** Internal structure of the scanning head of the PRCM. **c** The optical system design of the scanning head. The magnification of relay telescope was 3.15 which was calculated by dividing the focal length of the scanning lens by the focal length of the tube lens. The diameter of the multimode fiber is 25 μm, and the numerical aperture is 0.1. MEMS: microelectromechanical system; PBS: polarized beam splitter

Characterization of the PRCM

The USAF Resolving Power Test Target was used to test the field of view of the PRCM. It was put on the object stage and scanned by the PRCM to obtain images. The width of each line was known according to the USAF1951 resolution test chart. The field of view was calculated based on the width of a single pixel and pixel number.

Slides coated with gold nanoparticles were used to test the resolution of the PRCM. Images of the slide were taken by the PRCM. The pixels of smaller gold particles (R_{sample}) were recorded, and the number of pixels contained in the half-height and half-width (N_{sample}) was counted. The resolution of the PRCM (R) is calculated as

$$R = R_{\text{sample}} \times N_{\text{sample}}.$$

Next, the scanning speed of the PRCM was tested. The vibration frequency of the fast axis (F) and duty ratio of the slow axis (n) were recorded by the MEMS. The row number contained in each image taken by PRCM (h) was known as 660. Therefore, the scanning speed of the PRCM system (V) could be calculated using the following calculation:

$$V = F \times n/h.$$

To test the imaging depth of the PRCM, images of mouse and human normal skin were captured by tomography using the PRCM. The images of different layers of the skin were compared with a histopathologic map of human skin. Then, depth information corresponding to different layers of the skin tissue was known, and the imaging depth of the PRCM was set up.

According to the Nyquist sampling law, the optical section thickness is half of the axial resolution. The axial resolution was therefore evaluated by the axial response function test, which is known as the point spread function (PSF). The axial resolution test system is shown in Fig. S2 (Supplementary Information). A 40× water immersion objective was

used as the imaging objective, and water was used as the medium. Then, the silicon reflector was scanned for imaging to measure the axial resolution. The axial movement of the nanostage was controlled by the software. Starting from the initial test position, images were saved every step of 1 μm to obtain a set of images with various light intensities (Fig. S3 in Supplementary Information). ImageJ software was used to measure the gray value of the RCM images with fixed pixels.

The Gaussian curve is the axial response function curve, which shows the distribution of the light intensity along the axial direction in the center of the image, that is, the axial PSF.

Then, the Gaussian beam normal distribution formula is calculated as

$$f(x) = \frac{1}{\sqrt{2\pi}\sigma} e^{\frac{-(x-\mu)^2}{2\sigma^2}},$$

where μ is the mean of a normally distributed random variable x, and σ^2 is the variance of the random variable x. The Gaussian fitting curve equation is calculated by Origin software:

$$f(x) = \frac{A}{w\sqrt{\pi/2}} e^{-2\left(\frac{x-x_c}{w}\right)^2},$$

where x_c is equivalent to μ, w is the double of the standard deviation, and the formula is converted to

$$\sigma = \frac{1}{2}w.$$

The full width at half maxima (FWHM) is calculated as

$$\mathrm{FWHM} = 2\sqrt{2\ln 2}\sigma = \sqrt{2\ln 2}w.$$

Isolation and cultivation of mesenchymal stem cells derived from umbilical cords (UC-MSCs)

All studies were performed according to the "Ethical Guiding Principles on Human Embryonic Stem Cell Research" (of the Ministry of Science and Technology and the Ministry of Health, People's Republic of China, 2003) and Helsinki Declaration. Five human umbilical cords were generously donated by mothers who delivered healthy babies by cesarean section from the First Affiliated Hospital of Soochow University. All donors signed the informed consent with ethical approval. UC-MSCs were isolated and cultured in vitro as previously reported [21]. The umbilical cord vessels and outer membrane were removed, and mesenchymal tissue in Wharton's jelly was dissected. Then, the tissues were cut into small pieces and inoculated in culture dishes with a diameter of 10 cm. Dulbecco's Modified Eagle Medium/Nutrient Mixture F-12 (DMEM/F12 medium, Gibco, C11330500BT, USA) supplemented with 10% fetal bovine serum (FBS, Gibco, USA) and 1% penicillin–streptomycin was added to the dish and changed every 3 days. The cells were passaged when they reached 90% confluence. UC-MSCs cultured for fewer than five passages were used in the experiments for this study.

UC-MSC differentiation assays

The osteogenic and adipogenic differentiation abilities of UC-MSCs were evaluated by Alizarin Red and Oil Red O staining, respectively. For osteogenic differentiation, UC-MSCs were cultured with OriCellTM Osteogenic Differentiation Medium (Cyagen, HUXMA-90021, China). Osteogenic differentiation of UC-MSCs was assessed on day 21 using Alizarin Red staining for calcium nodules in mature osteocytes (VivaCell Biosciences, C37C00150, USA). For adipogenic differentiation, UC-MSCs were cultured with MesenCultTM Adipogenic Differentiation medium (Stem Cell Tech., 05412, Canada). Adipogenic differentiation of UC-MSCs was assessed on day 14 by qualitative Oil Red O staining for lipid-filled mature adipocytes (VivaCell Biosciences, C37A00150, USA). Images were taken using an inverted NIB410 microscope (Nexcope, China).

Wound model preparation and cell transplantation

All animal procedures were conducted according to the guidelines of the Animal Welfare Committee of Suzhou Institute of Biomedical Engineering and Technology, Chinese Academy of Sciences (SIBET, CAS). Eight- to sixteen-week-old Balb/C mice were used in the experiments of this study. An excisional skin wound model was generated as reported [22]. First, furs on the mouse back were removed, and then, a full thickness excisional wound with a diameter of 8 mm was made using a biopsy punch. Twelve mice with wounds were then randomly divided into two groups. A total of 20 μL 50% saline/Matrigel (356231, Corning, USA) alone (control) or 1×10^6 dissociated UC-MSCs resuspended with 20 μL 50% saline/Matrigel (MSCs) were applied to each group of wounds, which were immediately covered with a transparent antibacterial wound dressing (3M, Germany). Images of the wounds were taken on days 0, 4, 7, 10, 14, 18, and 24 post-treatment. The wound sizes were measured and analyzed by analyzer software (ImageJ).

Reflectance confocal imaging of skin and skin wounds in vivo

PRCM was used to evaluate the skin of mice and humans. For mice, the animal was anesthetized using isoflurane after the removal of hair. The skin was kept moist by adding water onto

the back of the mouse. To obtain clear images, the ultrasonic coupling agent was smeared onto the objective lens in the scanning head of the PRCM. Then, the scanning head was placed onto the skin, and the step distance of the stepping motor was adjusted to obtain clear images of the stratum epidermis and cutaneous appendages. For observation of skin wounds, the scanning head was first placed onto normal skin around the wound to set up an appropriate step distance and then moved to the edge of the wound and the center of the wound. Images were taken on days 0, 7, 17, and 24 after wound preparation.

Histological and immunofluorescent examination

Mice were killed on days 7, 17, and 24 after wound preparation. Skin samples from the wound sites with some surrounding skin were dissected and fixed with 4% paraformaldehyde overnight at 4 °C and then processed for paraffin embedding. For hematoxylin and eosin (H&E) staining, tissue sections were deparaffinized, rehydrated and stained with hematoxylin and eosin. For Masson trichrome staining, tissue sections were stained with hematoxylin, acid ponceau, and aniline blue. For immunofluorescence staining, the tissue sections were deparaffinized, rehydrated and incubated with rabbit anti-cytokeratin 14 (Abcam) antibody and visualized with Alexa-488-conjugated donkey anti-rabbit antibody (Abcam). DAPI was used for counterstaining nuclei. Images were captured by a Leica TCS SP5 confocal microscope or DMetrix wide-field microscope.

Statistical analysis

Numerical data are shown as the means ± standard deviations. Two-tailed Student's t tests or one-way ANOVA was used to indicate differences among groups. The asterisk was used to denote $p<0.05$ and considered significant. $p>0.05$ (ns) indicated that the difference was not significant.

Results

Development of the PRCM

We designed PRCM that could be used for nonintrusive and point-of-care testing for skin observations. This device displayed grayscale images with varying degrees of light and shade based on the different refractive indexes of the microstructures in the skin tissue, such as melanin, oxygenated hemoglobin, and organelles. As shown in Fig. 1, the PRCM consisted of a scanning head, electric control panel, and master computer. The working process of the scanning head, which was a key component of the PRCM, is shown in Figs. 2a and 2b and described below.

The 830 nm laser was introduced into the system through a single-mode polarization-maintaining fiber, and the laser beam was collimated by a collimating lens. Through a PBS, the S-polarized light was then reflected to the MEMS and produced two-dimensional scanning at high speed within a certain optical angle (Fig. S1 in Supplementary Information). The beam was then expanded by a scanning lens and a field mirror. The polarized light of the beam was modulated by a quarter wave plate. Finally, the beam was focused on the experimental sample by the objective lens after reflecting off mirror 1. The sample reflection beam was then returned through the original path, passing through the objective lens, mirror 1, quarter wave plate, field mirror, scanning lens, MEMS, and finally PBS. Since the laser passed through the quarter wave plate twice, the polarization direction was reverted from S-polarized light to P-polarized light. The P light passed through the PBS, refracted through mirror 2, passed through the pinhole lens, and focused on a multimode fiber. A confocal pinhole was formed in the optical fiber ports of the multimode fibers.

Next, the light was filtered by the pinhole and directed into an external avalanche diode by the optical fiber. The avalanche diode converted optical signals to electrical signals. Confocal images were reconstructed after signal acquisition by the data acquisition board. Imaging of samples from the surface layer to deep layers was achieved by adjusting the axial focusing device at the objective lens.

To produce PRCM, a compact design of the optical system was the first and key step, which was also the premise for the design of the mechanical system. The dimensions of each optical element and the distances between components are shown in Fig. 2c, and some optical parameters were calculated based on the following parameters.

An objective lens (Olympus, Japan) with a magnification (N) of 40× was used for our PRCM. The focal length (f_{obj}) of the objective lens was 4.5 mm, while the numerical aperture (NA) was 0.8. The entrance pupil diameter of the objective lens (D) is calculated as

$$D = 2 \times f_{\mathrm{obj}} \times \tan\theta = 2 \times f_{\mathrm{obj}} \times \mathrm{NA} = 7.2\,\mathrm{mm}.$$

The focal lengths of the scanning lens (f_{s}), field mirror (f_{t}), and pinhole lens (f_{p}) were 20, 63, and 25 mm, respectively. The field of view for the viewable section (S_{obj}) was set to 0.5 mm×0.5 mm, and the length of the viewable section (L_{obj}) was set to 0.5 mm. The length of the field of view for the main image plane (L) can be calculated as follows:

$$L = L_{\mathrm{obj}} \times \left(f_{\mathrm{t}}/f_{\mathrm{obj}}\right) = 0.5 \times (63/4.5) = 7\,\mathrm{mm}.$$

The field angle of the scanning lens (θ_{S}) can be calculated as

$$\theta_{\mathrm{S}} = \arctan(L/f_{\mathrm{s}}) = \arctan(7/20) = 19.3^{\circ}.$$

The field angle of the field mirror (θ_f) can be calculated as

$$\theta_f = \arctan(L/f_t) = \arctan(7/63) = 6.3°.$$

The rotation angle of MEMS (θ_{MEMS}) can be calculated as follows:

$$\theta_{MEMS} = 0.5 \times \arctan(0.5L/f_s) = 0.5 \times \arctan(0.5 \times 7/20) = 5°.$$

The ideal swing angle for the fast and slow axes of the MEMS was ±5°. However, the motion of the slow axis was forced by a sawtooth wave, and the actual swing angle of the slow axis was measured at ±3.4°. The motion of the fast axis was forced by a sine wave, and the actual swing angle of the fast axis was measured at ±5.3°. The field of view on the slow axis (V) is calculated as

$$V = 2 \times \left[\tan\left(2 \times \theta_{MEMS}^{Y}\right) \times f_s \times (f/f_t)\right] \approx 343\,\mu m.$$

The field of view on the fast axis (H) is calculated as

$$H = 2 \times \left[\tan\left(2 \times \theta_{MEMS}^{X}\right) \times f_s \times (f/f_t)\right] \approx 532\,\mu m.$$

The field of view of the PRCM system was 343 μm× 532 μm.

A confocal pinhole was formed in the optical fiber ports of the multimode fibers. The diameter of the pinhole ($\Phi_{Pinhole}$) is calculated as follows:

$$\Phi_{Pinhole} = \frac{1.22 \times \lambda}{NA} \times N = \frac{1.22 \times \lambda}{NA} \times \frac{f_t}{f_{obj}} \times \frac{f_p}{f_s} = 22.2\,\mu m,$$

where λ is the laser wavelength with the value of 830 nm. The pinhole diameter of 0.7–1.5 airy spot can be used to maintain the imaging capability of the system; so, the available multimode fiber with the diameter of 25 μm was employed in the PRCM.

Based on the optical path design, all the above optical elements were assembled in a handheld shell. The total weight of the PRCM was 0.7 kg, with dimensions of 200 mm in length, 80 mm in height, and 70 mm in width which made it convenient to use in the clinic.

Characterization of the PRCM

To investigate whether the PRCM could be used to examine different layers of skin tissue, key characterizations of the PRCM were evaluated. First, the field of view of the PRCM was examined using the USAF1951 resolution test chart. As shown in Fig. 3a, the red line marks the second line pairs in group 6 in both the lateral and axial directions. The number of line pairs was 17.96 lp/mm (line pair/millimeter) according to the USAF resolving power test target 1951 (Table S1 in Supplementary Information). Therefore, the line width was 27.8 μm. The red line intersected three black lines and two white lines (5 lines in total), and the total width was 139 μm, which comprised 266 pixels (Fig. 3b). The width per pixel was then calculated to be 0.52 μm. Each image contained 1024 pixels horizontally, which indicated that the lateral field of view was 532 μm. Based on similar calculations, the longitudinal field of view was 343 μm. The field of view of the PRCM system was determined to be 343 μm×532 μm, which was consistent with our hypothesis during the design of the system.

Next, imaging resolution was measured using gold particles with a diameter of 100 nm. White dots represent gold particles in the left image of Fig. 3c, while the pixels contained in the squared dots are shown in the right chart of Fig. 3c, which represent 7 pixels. As the width of each pixel was 0.13 μm, the imaging resolution was 0.91 μm.

To determine the scanning speed of the system, the vibration frequency of the fast axis (F=12 kHz) and duty ratio of the slow axis (n=0.68) were recorded by the MEMS (Fig. 3d). As each image contained 1024 frames, the scanning speed was calculated as 8 frames/s.

To determine the light wavelength for the PRCM, the absorption coefficients of hemoglobin, water, and melanin were tested under different wavelengths. A wavelength of 830 nm was chosen as the appropriate light wavelength, as the absorptivity of different components at this wavelength was the highest significant.

The PSF was evaluated to measure the optical section thickness of the PRCM. Select the pixel point in the image X=360, Y=230 to perform a Gaussian fit (Fig. 3e). The FWHM was calculated as 5 μm, which was also defined as the axial resolution. Therefore, the axial resolution is approximately 5 μm. According to the Nyquist sampling law, the optical section thickness of the PRCM is 2.5 μm. The measured characteristics of the PRCM suggested its potential to be used as an imaging tool.

Visualization of mouse skin using the PRCM

Next, we wondered whether normal mouse skin could be visualized by the PRCM, which was the precondition for nonintrusive testing of skin wounds. Mouse skin was scanned using the PRCM after removal of hair. Mouse skin is composed of epidermis, dermis and subcutaneous tissue, while the epidermis is divided into the strantum corneum, stratum granulosum, stratum spinosum and stratum basale from superficial to deep. Additionally, the stratum corneum is composed of flattened keratinocytes with highly reflective keratin in the cytoplasm. PRCM evaluation showed that the stratum corneum displayed large, bright, polygonal anucleated cells

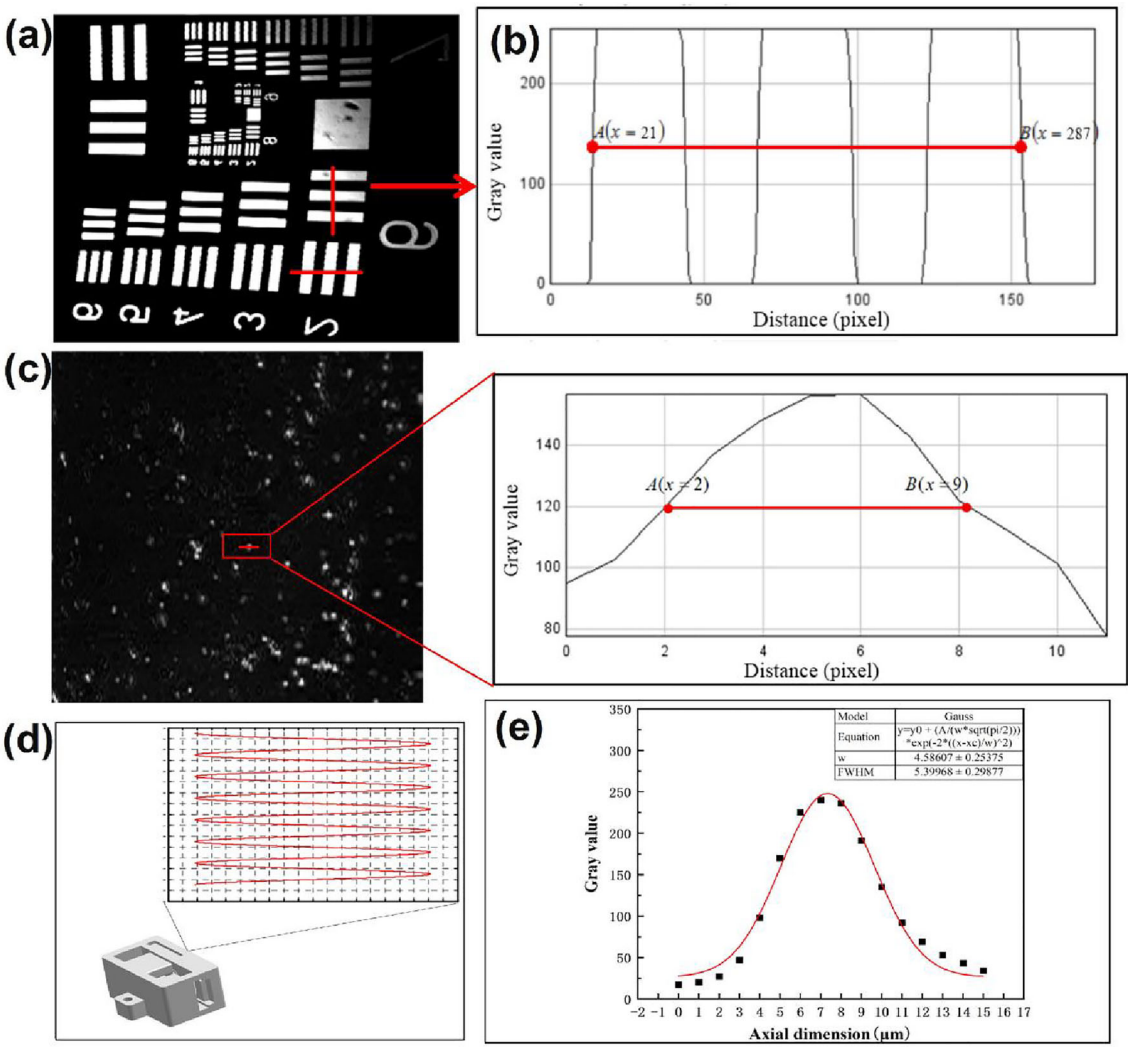

Fig. 3 Characterization of the portable reflectance confocal microscope (PRCM). **a** Tests of field of view for the PRCM using USAF resolving power test target 1951. The resolution was characterized by black and white stripes and the red line marked the second line pairs in group 6 in the lateral and axial directions. **b** The pixels contained in the second line pairs in group 6. The red line crossed 266 pixels (287 minus 21). **c** Tests of imaging resolution for the PRCM using 100 nm gold particles. White dots represent gold particles in the left picture. The gray value and the pixels contained in the squared dots are shown in the right chart (7 pixels; 9 minus 2). **d** Tests of scanning speed for the PRCM. The vibration frequency of the fast axis and duty ratio of the slow axis were recorded by the microelectromechanical system (MEMS). The red curve represents the tracking of the laser spot after passing through the MEMS galvanometer. **e** Axial response function curve. The Gaussian curve is the axial response function curve, which shows the light intensity distribution along the axial direction of a pixel in the image

(Fig. 4a). Skin folds with lower reflectance were revealed as dark lines among clusters of keratinocytes (marked by the blue triangle in Fig. 4a). The stratum granulosum had reflective keratohyalin granules in the cytoplasm and ovoid nuclei in the center. Dark central oval-shaped nuclei and bright cytoplasm arranged in a typical honeycomb pattern were displayed under the PRCM (marked by the red circle in Fig. 4b). The stratum spinosum was composed of polyhedral keratinocytes that were joined together with desmosomes. Cells are smaller in the stratum spinosum than cells in the stratum granulosum. Therefore, the PRCM imaging showed a honeycomb pattern with smaller dark nuclei in the stratum spinosum (marked by the dotted red circle in Fig. 4c). The stratum basale was a single layer of columnar keratinocytes. As the nucleus is large, ovoid, and occupies most of the cell, low grayscale regions were seen under the PRCM. The epidermis is tightly connected to the dermis, and finger-like projections called papillae from the dermis extend toward the epidermis. Horizontal images provided dark and round centers surrounded by bright basal keratinocytes (marked by the green circle in Fig. 4d).

Owing to the characteristic shapes and keratin content, all of the skin layers could be clearly visualized with different grayscale and patterns by using the self-developed PRCM.

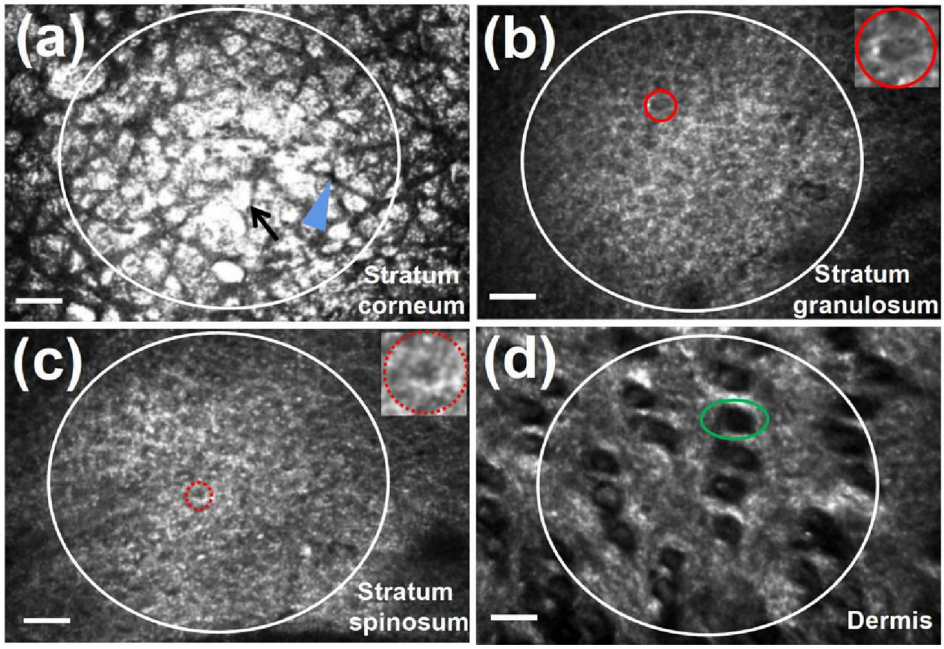

Fig. 4 The stratum corneum, stratum granulosum, stratum spinosum, and papillary dermis of mouse back skin were visualized by using the portable reflectance confocal microscope (PRCM). Bright filed of the PRCM is marked by a white circle in each image. **a** Stratum corneum with the depth of 20–35 μm; arrow indicates keratin, blue triangle indicates skin fold. **b** Stratum granulosum as shown by a red circle, was with the depth of 40–70 μm. **c** Stratum spinosum marked by dotted red circle, was with the depth of 80–100 μm. **d** Papillary dermis was with the depth of 130–150 μm; a green circle marked the dermal papilla. Scale bar: 50 μm

Tracing of cutaneous wound healing using the PRCM in a noninvasive way

RCM allows for noninvasive, in vivo evaluation of the skin with cellular resolution. To determine whether the newly developed PRCM could be applied to monitor skin wound healing, PRCM evaluation was compared to histological analysis (Fig. 5a). UC-MSCs (Fig. S4 in Supplementary Information) were applied to the skin wounds in the MSC group, while the control group was treated with saline.

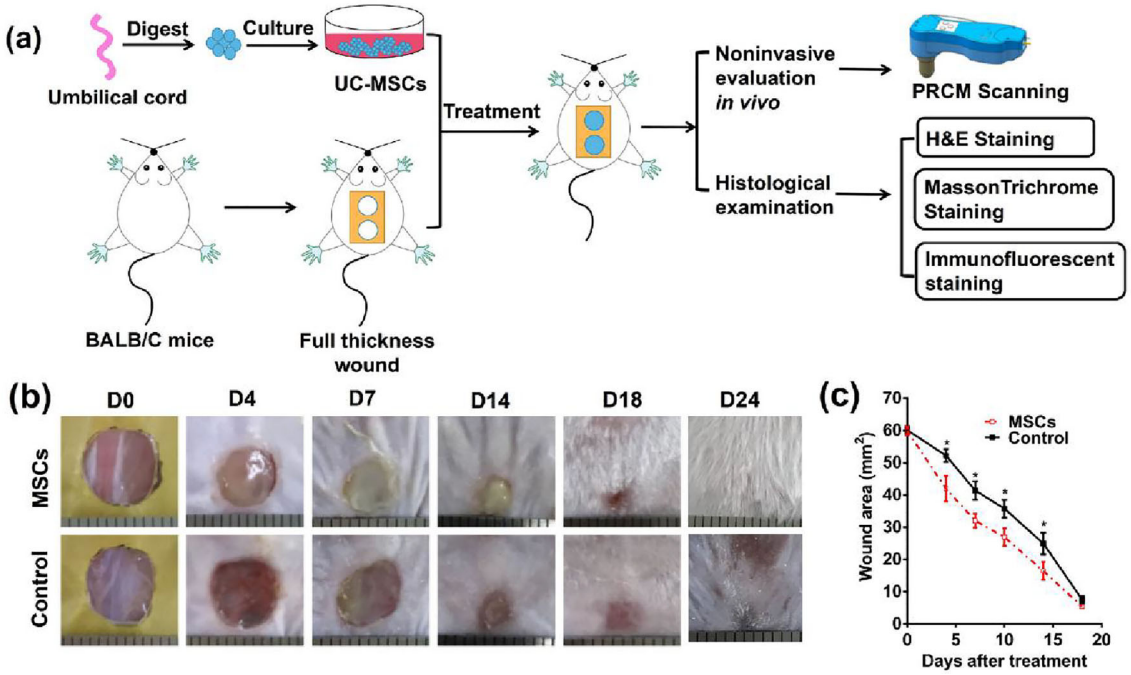

Fig. 5 Mesenchymal stem cells (MSCs) accelerated skin wound healing. **a** The experimental design for the comparison of portable reflectance confocal microscope (PRCM) evaluation and histological analysis. **b** Representative images of the mouse wound treated with MSCs or control. **c** Analysis of changes in wound size (mm^2) of the two groups showed that MSCs significantly accelerated wound healing (n=5)

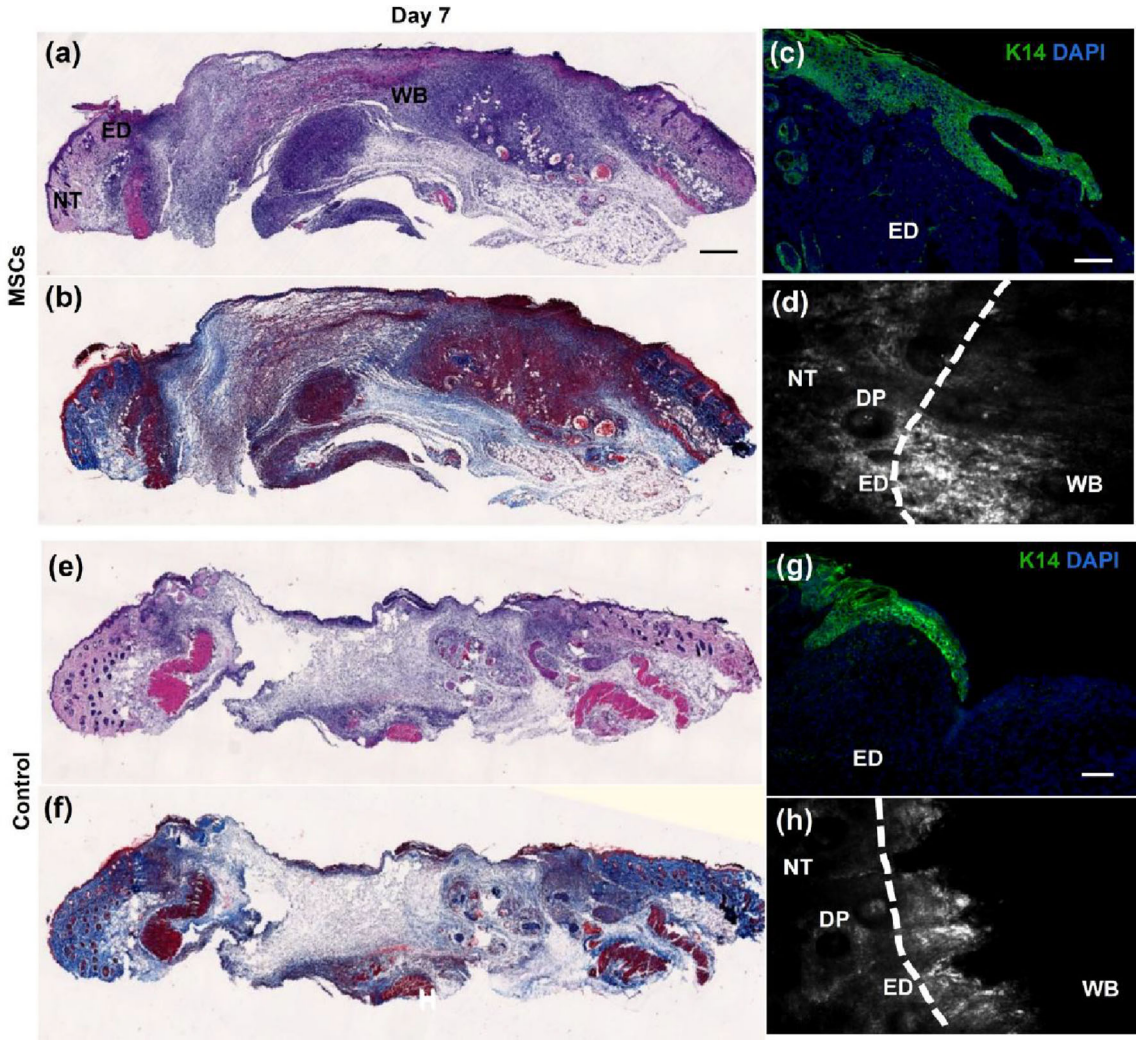

Fig. 6 Monitoring of the early-stage wound healing using the portable reflectance confocal microscope (PRCM). Wound sections on day 7 post-MSC treatment were stained with H&E (**a**) and Masson trichrome (**b**) for general observation of the skin wound. Scale bar: 200 μm. Immunofluorescent staining against K14 (**c**) was performed for observation of epidermis regeneration. Scale bar: 50 μm. In vivo PRCM evaluation showed matrix deposition on skin wound 7 days post-MSC treatment (**d**). Wound sections on day 7 post-saline treatment were stained with H&E (**e**) and Masson trichrome (**f**). Scale bar: 200 μm. Epidermis regeneration revealed by immunofluorescent staining against K14 (**g**). Scale bar: 50 μm. PRCM showed dark zones in the control group (**h**). MSC: mesenchymal stem cell; NT: normal tissue; ED: wound edge; WB: wound bed; DP: dermal papilla

Images of wound healing in the two groups are shown at different time points (Fig. 5b). Analysis of wound areas demonstrated that the MSC treatment significantly promoted skin wound healing when compared with the control group (Fig. 5c).

On day 7, H&E staining showed thicker tissue layers and better-formed granulation tissue in the MSC-treated group than in the control group (Figs. 6a and 6e). Furthermore, Masson trichrome staining revealed greater collagen deposition in wound bed (WB) treated with MSCs than in the control group at the same time point, indicating that MSCs increased matrix protein recruitment (Figs. 6b and 6f). Immunofluorescent staining against K14 (an epidermal progenitor cell marker) revealed that K14-positive epithelium was observed at the wound edge (ED) in both the MSC-treated group and the control group (Figs. 6c and 6g). The PRCM was then used to observe skin wound healing in the two groups. When dermal papillae (DP) were seen under PRCM on the normal tissue (NT), the scanning head was moved from NT to the wound edge (ED) and wound bed (WB). On day 0, dark zones without any cellular structure were seen in both groups, as the full thickness of skin was removed (data not shown). On day 7, low grayscale structures were observed at the wound edge (ED) in the MSC group, while dark zones were seen in the control group (Figs. 6d and 6h), confirming the difference in matrix deposition as shown by H&E and immunostaining.

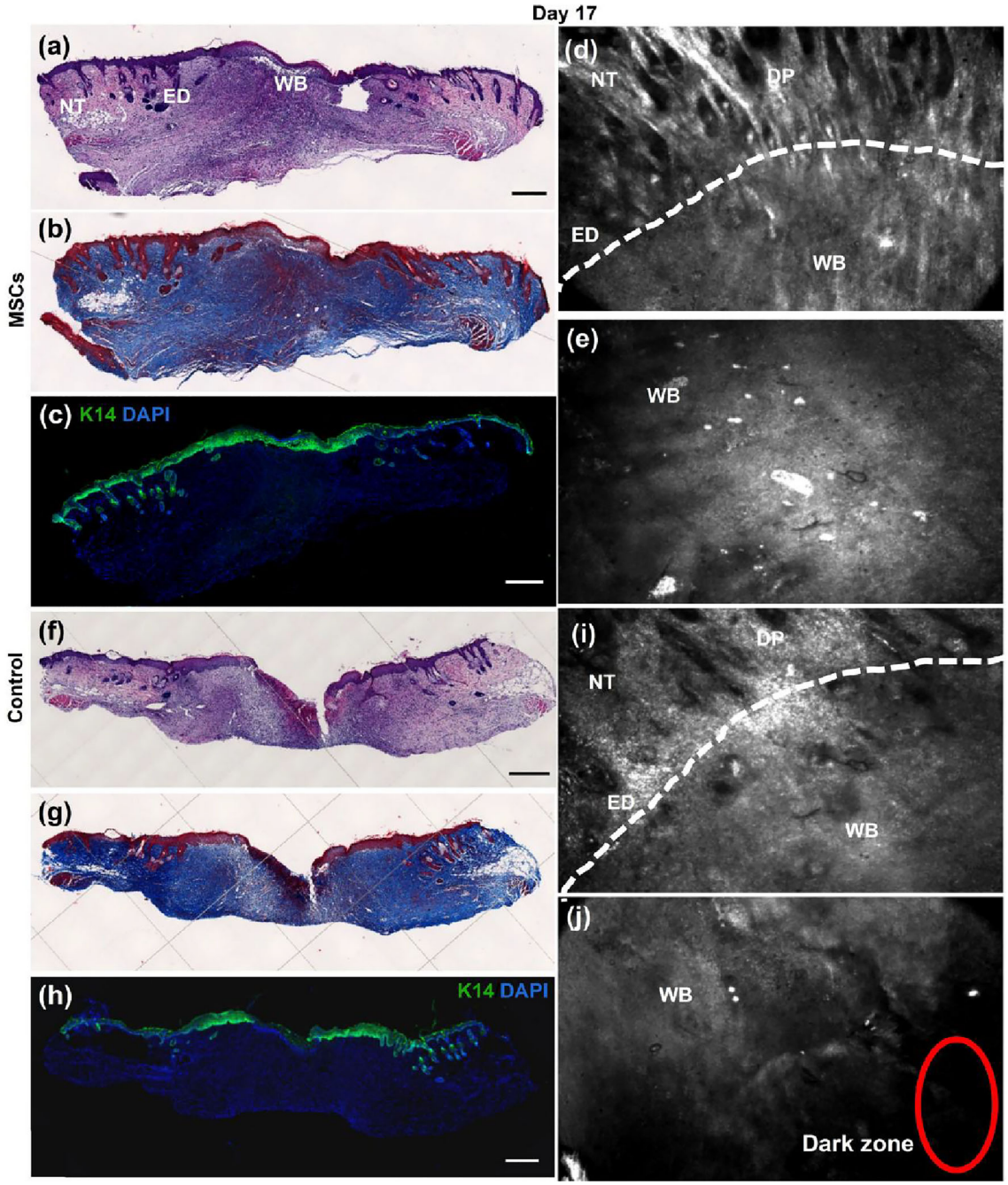

Fig. 7 Evaluation of epidermis regeneration during wound healing using the portable reflectance confocal microscope (PRCM). Wound sections on day 17 post-MSC treatment were stained with H&E (**a**) and Masson trichrome (**b**) for general observation of the skin wound. Scale bar: 200 μm. Immunofluorescent staining against K14 (**c**) was performed for observation of epidermis regeneration. Scale bar: 100 μm. In vivo PRCM observation showed epidermis regeneration on the skin wound edge (**d**) and wound bed (**e**) 17 days post-MSCs treatment. Wound sections on day 17 post-saline treatment were stained with H&E (**f**) and Masson trichrome (**g**). Scale bar: 200 μm. Epidermis regeneration was observed by immunofluorescence staining against K14 (**h**). Scale bar: 100 μm. PRCM imaging showed low grayscale zones in the wound edge (**i**) and dark zones in the center of wound bed in the control group (**j**). MSC: mesenchymal stem cell; NT: normal tissue; ED: wound edge; WB: wound bed; DP: dermal papilla

The detection of different grayscale values in the wound bed made it possible for PRCM to evaluate the wound healing process at a very early stage.

On day 17, H&E staining showed that the wounds were fully covered in the MSC-treated group (Fig. 7a), while there were still gaps in the wounds of the control group

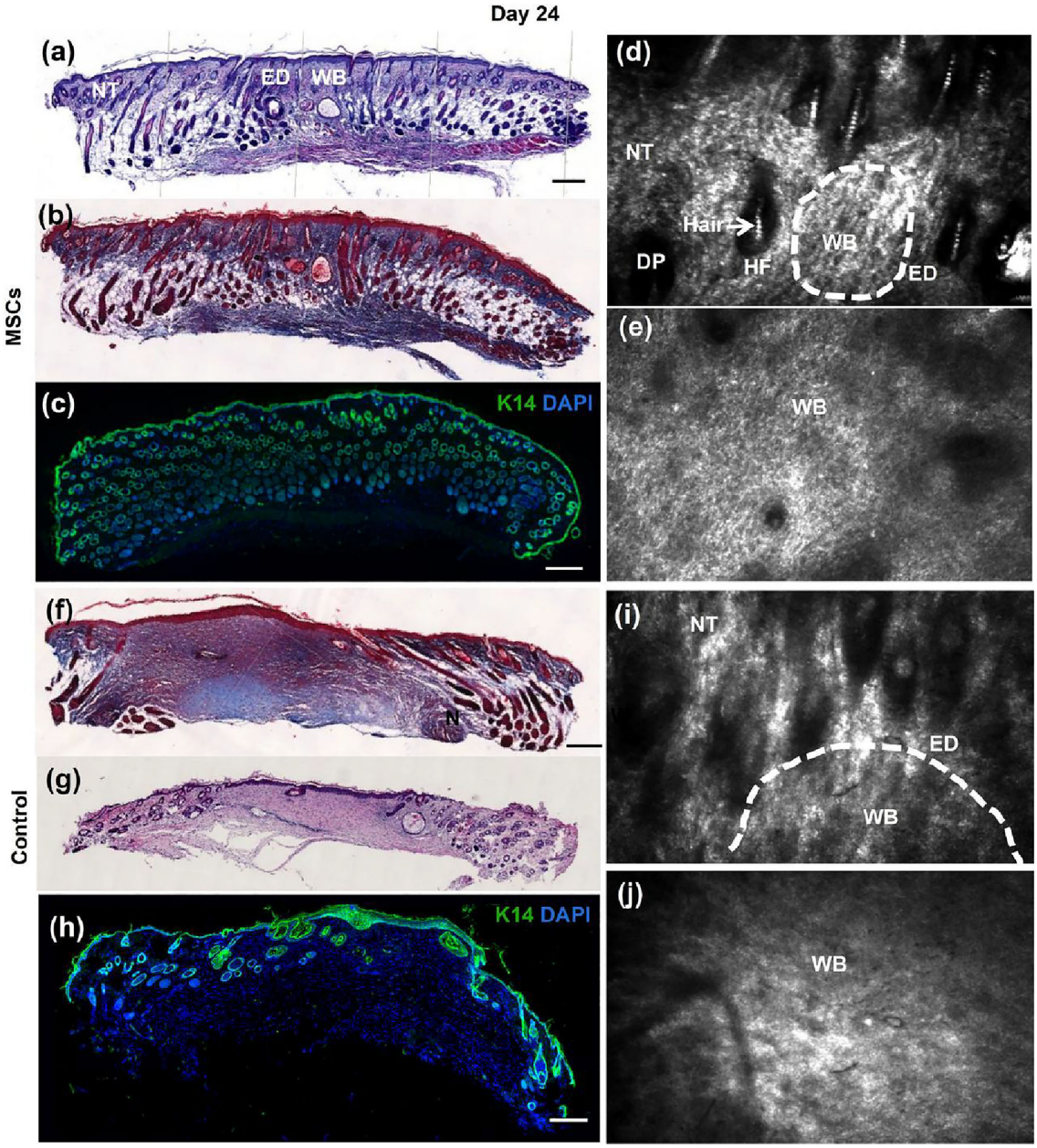

Fig. 8 Portable reflectance confocal microscope (PRCM) evaluation of hair follicle regeneration was comparable to histological analysis. Wound sections on day 24 post-MSC treatment were stained with H&E (**a**) and Masson trichrome (**b**) for general observation of the skin wound. Scale bar: 200 μm. Immunofluorescent staining against K14 (**c**) was performed for observation of epidermis and skin appendage regeneration. Scale bar: 100 μm. In vivo PRCM evaluation showed epidermis and hair follicle regeneration on the skin wound edge (**d**) and wound bed (**e**). Wound sections on day 24 post-saline treatment were stained with H&E (**f**) and Masson trichrome (**g**). Scale bar: 200 μm. Epidermis regeneration was observed by immunofluorescent staining against K14 (**h**). Scale bar: 100 μm. PRCM evaluation displayed DP in the wound edge (**i**) and a honeycomb pattern in wound bed (**j**). MSC: mesenchymal stem cell; NT: normal tissue; ED: wound edge; WB: wound bed; HF: hair follicle; DP: dermal papilla

(Fig. 7f). Masson trichrome staining revealed that collagen was distributed throughout the wound (Fig. 7b) in the MSC group, and collagen was distributed all over the wound except the gap area (Fig. 7g) in the control group, indicating that the MSCs promoted more significant wound healing. Immunofluorescent staining against K14 was then performed to evaluate the re-epithelialization effects of MSCs. K14-positive cells were found throughout the whole wound bed in the MSC group (Fig. 7c), while a K14-negative gap was seen in the wound center of the control group (Fig. 7h). When PRCM was applied to observe wound healing, low grayscale zones with honeycomb-like cell structures were seen in the

wound bed of the MSC group (Figs. 7d and 7e), while low grayscale areas with dark zones were found in the wound bed of the control group (Figs. 7i and 7j). These observations suggest that the dark gap seen using the PRCM revealed a lack of epidermal regeneration, which correlated with histological staining.

The PRCM was then used to evaluate late-stage wound healing. First, H&E (Fig. 8a) and Masson trichrome staining (Fig. 8b) were performed on day 24 after MSC treatment, which showed complete re-epithelization and skin appendage regeneration. K14-positive cells were seen in the epidermal layer and the skin appendages of the wound based on immunofluorescent staining (Fig. 8c). The PRCM evaluation displayed dark dermal papillae (DP) and hair follicles (HF) with highly reflective hair shafts (hair) in the wound edge (ED), and honeycomb-like structures in the wound bed (WB) (Figs. 8d and 8e), which indicated complete wound healing in the MSC-treated group. In the control group, histological staining showed thick epidermal layers without appendages in the wound center, which indicated incomplete remodeling of the skin wound (Figs. 8f–8h). Consistent with these observations, PRCM imaging revealed low grayscale areas without hair follicles and highly reflective hair shafts in the wound bed (Figs. 8i and 8j). These data demonstrate that PRCM was consistent with histological evaluation and could be used for detection of the remodeling stage of wound healing.

PRCM displayed great potential to detect collagen rebuilding, epidermal reconstitution, and hair follicle regeneration noninvasively during wound healing. These results indicate the possibility for PRCM to be used as a noninvasive method to observe wound healing at different stages.

Human skin visualized with the PRCM akin to histological analysis

To investigate whether the PRCM can be used for the evaluation of human skin diseases in the clinic, PRCM images of human arm skin were compared to the skin biopsy with histological staining. Human skin is composed of the epidermis and dermis, and the epidermis is subdivided into the stratum corneum, stratum granulosum, stratum spinosum, and stratum basale, which is similar to mouse skin. To display all cell layers of the skin, H&E staining of sagittal sections of human skin was performed and shown in Fig. 9a. As the PRCM displayed horizontal images, H&E staining was then performed on cross sections of human skin samples. The stratum corneum layer, composed of flattened keratinocytes without nuclei or cell organelles, was seen under H&E staining (Fig. 9b), while the PRCM displayed large, bright polygonal and anucleated cells. Skin folds with low reflectance appeared as dark spaces among clusters of keratinocytes (marked by the blue triangle in Fig. 9b′). The stratum granulosum cells with reflective keratohyalin granules in the cytoplasm and ovoid nuclei in the center were observed by H&E staining (Fig. 9c), while dark central oval-shaped nuclei surrounded by bright cytoplasm were arranged in a typical honeycomb pattern by PRCM evaluation (marked by the red circle in Fig. 9c′). The stratum spinosum was composed of polyhedral keratinocytes, which were shown by H&E staining (Fig. 9d). This layer also showed a honeycomb pattern but contained smaller cells than the stratum granulosum by the PRCM evaluation (marked by the dotted red circle in Fig. 9d′). The stratum basale at the dermoepidermal junction was arranged in ring-like structures surrounding dermal

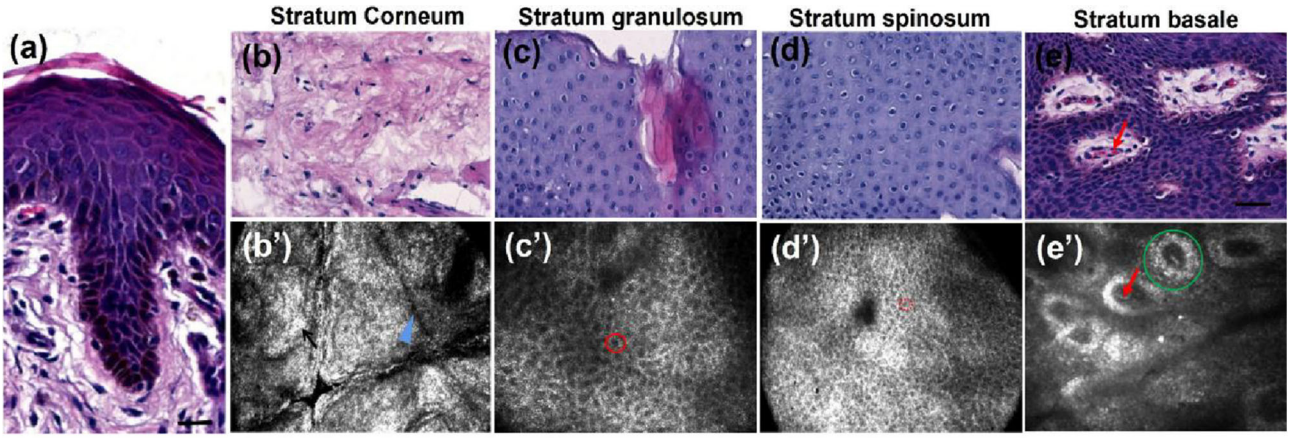

Fig. 9 Comparative features of human skin using portable reflectance confocal microscope (PRCM) and histopathology. **a** H&E staining on sagittal sections of human skin. H&E staining on cross-sectional images of the stratum corneum (**b**), stratum granulosum (**c**), stratum spinosum (**d**) and the stratum basale (**e**). Human arm skin was evaluated in vivo using the PRCM. **b'** Stratum corneum; black arrow indicates keratin, blue triangle indicates a skin fold. **c'** Stratum granulosum as shown by the red circle. **d'** Stratum spinosum marked by a dotted red circle. **e'** Stratum basale: a green circle marked the dermal papilla and a red arrow pointed to the blood cells in capillaries of the dermal papilla. Scale bar: 50 μm

papilla in the center (Fig. 9e), while the stratum basal keratinocytes with randomly scattered melanocytes (with high reflective melanin) formed a bright ring around the dermal papilla under PRCM imaging (Fig. 9e′). In the center of each papillae, blood flow within capillaries could be observed by H&E staining and by PRCM evaluation (marked by the red arrow in Figs. 9e and 9e′).

In this study, we showed the applicability of the newly developed PRCM for monitoring the processes involved in wound healing. The PRCM enabled the detection of re-epithelization, wound closure by the newly formed epidermis, and skin appendage regeneration. Using the PRCM, different stages of wound healing could be monitored noninvasively and in real time.

Discussion

Nonhealing wounds affect millions of people worldwide [23]. Wound healing represents a complex process involving the interaction of keratinocytes, fibroblasts, and inflammatory cells in three classic stages. Effective monitoring of the wound healing process can lead to better treatments and quicker healing [24].

Traditional biopsy-based histopathologic analysis does not provide diagnosis in real time and may cause bleeding, infection or scarring [24], which leads to delays or failure in initiating adequate treatment [25]. Novel and precise diagnostic tools are currently needed for better monitoring of this process. Reflectance confocal microscopy (RCM) allows for the noninvasive detection of skin with cellular resolution in vivo [26]. Grayscale images in the horizontal plane can be obtained by RCM [27]. RCM has been successfully used in the diagnosis of key skin diseases, including melanoma [28] and keratinocyte carcinomas [29]. Handheld RCM, which allows free-form translation on the skin, has previously been used to assess treatment effects in facial lentigo maligna [30], delineate the margins of basal cell carcinomas, and check for recurrent extra mammary Paget's disease [31]. The VivaScope 3000 (Caliber ID, Rochester, NY, USA), a handheld reflectance confocal microscope used in many studies, is the only commercial handheld reflectance confocal microscope worldwide. The high price of the VivaScope 3000 limits its universal use, especially for clinics and practitioners that lack resources and service widespread rural populations.

The aim of this study was to design and develop a portable reflectance confocal microscope (PRCM) that could be used for noninvasive monitoring of the wound healing process. To reduce the weight and size of the PRCM, a microelectromechanical system (MEMS) was used instead of the traditional mechanical scanning galvanometer. Moreover, the small sizes of the scanning lens (20 mm) and pinhole lens (25 mm) were chosen for the PRCM, which were all assembled in a handheld shell. Based on the above design, the weight of the PRCM was kept at approximately 0.7 kg with dimensions of 200 mm×80 mm×70 mm. Furthermore, the optical resolution was measured as 0.91 μm, which was better than that of the VivaScope 3000. Due to the use of the MEMS, the scanning speed of the PRCM was 8 frames/s, which was faster than that of VivaScope 3000 (6 frames/s). The viewable section of the PRCM was calculated at 532 μm× 343 μm under 40× magnification, while the viewable section of VivaScope 3000 was 750 μm×750 μm under 30× magnification. All the above parameters of the PRCM were improvements or comparable to VivaScope 3000 (Table 1).

Table 1 Comparisons of commercial VivaScope 3000 and the newly designed PRCM

	VivaScope 3000	PRCM
Weight (kg)	0.7	0.7
Size (mm×mm×mm)	250×100×70	200×80×70
Optical resolution (μm)	Horizontal <1.25 in the center of the image field	Horizontal <0.91 in the center of the image field
	Vertical <5.0 in the center of the image field	Vertical <5.0 in the center of the image field
Maximum imaging depth	Superficial dermis	Superficial dermis
Viewable section (μm×μm)	Individual image 750×750	532×343
Image resolution (pixel)	1024×1024	1024×1024
Image digitization	8 bits	–
Frame rate (frame/s)	6	8
Imaging wavelength (nm)	830	830
Objective	Caliber ID StableView™ 30× magnification	Olympus, 40× magnification
	0.9 NA water immersion	0.8 NA water immersion

PRCM: portable reflectance confocal microscope; NA: numerical aperture

The maximum imaging depth of the PRCM was approximately 300 μm, which extends to the superficial dermis. The reticular dermis could be captured with the PRCM in skin with a thin epidermis, such as skin of the back and forearm. The superficial dermis was observed when the skin had a thick epidermis, such as the palm and plantar aspect. Moreover, PRCM images of different layers of the epidermis could be captured by adjusting the step motor, which demonstrated its potential for diagnosis and monitoring of skin diseases.

RCM has mostly been used for monitoring tissue damage induced by discoid lupus erythematosus, dermatitis, plaque psoriasis or cryosurgery injury [32–35]. Here, we extended the use of RCM to monitor the effects of topically applied MSCs on skin wounds by using our newly developed PRCM. We were able to evaluate the milestones of tissue repair noninvasively and in vivo with near-histological resolution by PRCM. Fibroblast and collagen fiber regeneration at the skin wound is the basis for favorable healing. PRCM visualization and H&E and Masson trichrome staining showed that MSCs promoted the formation of collagen fibers and fibrin. Epithelialization began with the migration of adjacent epidermal keratinocytes from the wound edges into the wound. PRCM allowed us to observe the epidermis with low grayscale at the wound edges and dark zones without epidermal cells at the wound center, as well as the migration of the epidermal tongue from the wound margin toward the wound bed over time. A large area of the low grayscale zone could be seen with the PRCM. At the maturation phase of wound healing, the epidermis regenerated with hair follicles in the MSC group, in which honeycomb-like structures and dark hair follicles with highly reflective hair shafts were observed using PRCM. A thick epidermis without skin appendages was seen in the control group at the same phase. Thus, different phases of wound healing could be well distinguished; the PRCM could be used as a noninvasive tool for the diagnosis and monitoring of skin wound healing in real time.

The active process of wound healing begins with an inflammatory reaction, including local vasodilatation and fluid extravasation into the extracellular space [36]. Epithelialization follows angiogenesis and begins with the migration of adjacent epidermal keratinocytes from the wound edges into the wound [35]. Visualization of immunocyte infiltration, angiogenesis, and circulation by PRCM will be the focus of our future studies.

Conclusions

In this work, the newly developed PRCM allows monitoring of the dynamic process of wound healing noninvasively and in real time. As the needs of the wound care market grow rapidly, there is a great advantage to translating optical imaging discoveries into chronic or acute wound diagnosis and monitoring with speed, precision, real-time responsiveness and portability. The PRCM that we developed shows great potential in wound imaging for routine wound care in clinics in the very near future.

Supplementary Information The online version contains supplementary material available at https://doi.org/10.1007/s42242-022-00223-1.

Acknowledgements This work was funded by the National Key Research and Development Program of China (No. 2021YFA1101100), the Strategic Priority Research Program of the Chinese Academy of Sciences (No. XDA16020807), the Major Innovative Research Team of Suzhou, China (No. ZXT2019007), Suzhou Institute of Biomedical Engineering and Technology (SIBET) and Jilin City Science and Technology Cooperation Project (No. E0550104), Science and Technology Innovation Talents in Universities of Henan Province and Doctor of Entrepreneurship and Innovation Program of Jiangsu Province in the year of 2020.

Author contributions LXZ and XM contributed to conceptualization; LXZ, MJW and JWW contributed to methodology; AHS and YHZ contributed to investigation; LXZ contributed to writing—original draft; all authors contributed to writing—review and editing; LXZ, SY and JZZ contributed to funding acquisition; YHZ contributed to resources; SY and JZZ contributed to supervision.

Declarations

Conflict of interest The authors declare that they have no conflict of interest.

Ethical approval All institutional and national guidelines for the care and use of laboratory animals were followed. All experimental protocols involving animals were approved by the Institutional Animal Care and Use Committee and followed the procedure for Animal Experimental Ethical Inspection of Suzhou Institute of Biomedical Engineering and Technology, Chinese Academy of Sciences (SIBET, CAS[2018-A21]). All procedures followed were in accordance with the ethical standards of the responsible committee on human experimentation (institutional and national) and with the Helsinki Declaration of 1975, as revised in 2008. Informed consent was obtained from all patients and volunteers for being included in the study. All experimental protocols involving human samples were approved by the Medical Ethics Committee of the First Affiliated Hospital of Soochow University (2019-136).

References

1. Olsson M, Jarbrink K, Divakar U et al (2019) The humanistic and economic burden of chronic wounds: a systematic review. Wound Repair Regen 27(1):114–125. https://doi.org/10.1111/wrr.12683
2. Frykberg RG, Ba NJ (2011) Challenges in the treatment of chronic wounds. Adv Wound Care 4(9):560–582. https://doi.org/10.1089/wound.2015.0635
3. Sorg H, Tilkorn DJ, Hager S et al (2017) Skin wound healing: an update on the current knowledge and concepts. Eur Surg Res 58(1–2):81–94. https://doi.org/10.1159/000454919
4. Wilkinson HN, Hardman MJ (2020) Wound healing: cellular mechanisms and pathological outcomes. Open Biol 10:200223. https://doi.org/10.1098/rsob.200223
5. Cheng HM, Guitera P (2016) Systematic review of optical coherence tomography usage in the diagnosis and management of basal cell carcinoma. Br J Dermatol 173(6):1371–1380. https://doi.org/10.1111/bjd.14042
6. Bleicher B, Levine A, Markowitz O (2018) Going digital with dermoscopy. Cutis 102(2):102–105
7. Xiong YD, Ma S, Li X et al (2016) A meta-analysis of reflectance confocal microscopy for the diagnosis of malignant skin tumours. J Eur Acad Dermatol Venereol 30:1295–1302. https://doi.org/10.1111/jdv.13712
8. Elliott AD (2020) Confocal microscopy: principles and modern practices. Curr Protoc Cytom 92(1):e68. https://doi.org/10.1002/cpcy.68

9. Hjorth MK, Burian EA, Glud M et al (2021) Closing of surgical wounds on ala nasi with an autologous patch: a case series and in vivo wound imaging using reflectance confocal microscopy. Skin Res Technol 27(5):988–990. https://doi.org/10.1111/srt.13024
10. Kang HY, Bahadoran P (2012) Application of in vivo reflectance confocal microscopy in melasma classification. J Am Acad Dermatol 67(1):157–158. https://doi.org/10.1016/j.jaad.2012.02.046
11. Ulrich M, Kanitakis J, González S et al (2012) Evaluation of Bowen disease by in vivo reflectance confocal microscopy. Br J Dermatol 166(2):451–453. https://doi.org/10.1111/j.1365-2133.2011.10563.x
12. Ardigo M, Longo C, Gonzalez S (2016) Multicentre study on inflammatory skin diseases from the International Confocal Working Group: specific confocal microscopy features and an algorithmic method of diagnosis. Br J Dermatol 175:364–374. https://doi.org/10.1111/bjd.14516
13. Middelkamp-Hup MA, Park HY, Lee J et al (2006) Detection of UV-induced pigmentary and epidermal changes over time using in vivo reflectance confocal microscopy. J Invest Dermatol 126(2):402–407. https://doi.org/10.1038/sj.jid.5700055
14. Reingold RE, Monnier J, Ardigò M et al (2022) Real-time reflectance confocal microscopy of cutaneous graft-versus-host disease correlates with histopathology. Transplant Cell Ther 28(1):51.e1-51.e14. https://doi.org/10.1016/j.jtct.2021.09.014
15. Zor F, Karagoz H, Erdemir AT et al (2016) Reflectance confocal microscopy as a useful diagnostic tool for monitoring of skin containing vascularized composite allograft rejection: a preliminary study on rats. Microsurgery 36(2):144–151. https://doi.org/10.1002/micr.22419
16. Levine A, Markowitz O (2018) Introduction to reflectance confocal microscopy and its use in clinical practice. JAAD Case Rep 4(10):1014–1023. https://doi.org/10.1016/j.jdcr.2018.09.019
17. Yélamos O, Hibler BP, Cordova M et al (2017) Handheld reflectance confocal microscopy for the detection of recurrent extramammary paget disease. JAMA Dermatol 153(7):689–693. https://doi.org/10.1001/jamadermatol.2017.0619
18. Tsai HW, Wang PH, Tsui KH (2018) Mesenchymal stem cell in wound healing and regeneration. J Chin Med Assoc 81(3):223–224. https://doi.org/10.1016/j.jcma.2017.06.011
19. Maranda EL, Rodriguez-Menocal L, Badiavas EV (2017) Role of mesenchymal stem cells in dermal repair in burns and diabetic wounds. Curr Stem Cell Res Ther 12(1):61–70. https://doi.org/10.2174/1574888x11666160714115926
20. Xu Y, Hong Y, Xu M et al (2016) Role of keratinocyte growth factor in the differentiation of sweat gland-like cells from human umbilical cord-derived mesenchymal stem cells. Stem Cells Transl Med 5(1):106–116. https://doi.org/10.5966/sctm.2015-0081
21. Xie Y, Li Y (2010) Experimental study of human umbilical cord mesenchymal stem cell isolation, culture and biological characteristics. J Bengbu Med Coll 10:982–985
22. Rodriguez J, Boucher F, Lequeux C et al (2015) Intradermal injection of human adipose-derived stem cells accelerates skin wound healing in nude mice. Stem Cell Res Ther 6(1):241. https://doi.org/10.1186/s13287-015-0238-3
23. Gonzales K, Fuchs E (2011) Skin and its regenerative powers: an alliance between stem cells and their niche. Dev Cell 43(4):387–401. https://doi.org/10.1016/j.devcel.2017.10.001
24. Wang Y, Beekman J, Hew J et al (2018) Burn injury: challenges and advances in burn wound healing, infection, pain and scarring. Adv Drug Deliv Rev 123:3–17. https://doi.org/10.1016/j.addr.2017.09.018
25. Masson-Meyers DS, Andrade TAM, Caetano GF et al (2020) Experimental models and methods for cutaneous wound healing assessment. Int J Exp Pathol 101(1–2):21–37. https://doi.org/10.1111/iep.12346
26. Shahriari N, Grant-Kels JM, Rabinovitz H et al (2021) Reflectance confocal microscopy principles, basic terminology, clinical indications, limitations, and practical considerations. J Am Acad Dermatol 84(1):1–14. https://doi.org/10.1016/j.jaad.2020.05.153
27. Rajadhyaksha M, Marghoob A, Rossi A et al (2017) Reflectance confocal microscopy of skin in vivo: from bench to bedside. Lasers Surg Med 49:7–19. https://doi.org/10.1002/lsm.22600
28. Pogorzelska-Antkowiak A, Calik J (2021) Mimics of melanoma in reflectance confocal microscopy. Int J Dermatol 60(5):540–546. https://doi.org/10.1111/ijd.15306
29. Jain M, Pulijal SV, Rajadhyaksha M et al (2018) Evaluation of bedside diagnostic accuracy, learning curve, and challenges for a novice reflectance confocal microscopy reader for skin cancer detection in vivo. JAMA Dermatol 154(8):962–965. https://doi.org/10.1001/jamadermatol.2018.1668
30. Fraga-Braghiroli NA, Merati M, Rabinovitz H et al (2015) Reflectance confocal microscopy features of a clonal seborrheic keratosis that clinically and dermoscopically simulates melanoma. Dermatol Surg 41:662–665. https://doi.org/10.1097/dss.0000000000000354
31. Kim BJ, Park SK, Chang H (2014) The effectiveness of mapping biopsy in patients with extramammary Paget's disease. Arch Plast Surg 41(6):753–758. https://doi.org/10.5999/aps.2014.41.6.753
32. Lacarrubba F, Verzì AE, Caltabiano R et al (2019) Discoid lupus erythematosus: reflectance confocal microscopy features correlate with horizontal histopathological sections. Skin Res Technol 25(2):242–244. https://doi.org/10.1111/srt.12636
33. Kišonas J, Venius J, Grybauskas M et al (2021) Acute radiation dermatitis evaluation with reflectance confocal microscopy: a prospective study. Diagnostics 11(9):1670. https://doi.org/10.3390/diagnostics11091670
34. Marina A, Cecilia N, Francesco L et al (2017) Monitoring treatment response in psoriasis: current perspectives on the clinical utility of reflectance confocal microscopy. Psoriasis 7:27–34. https://doi.org/10.2147/ptt.s107514
35. Terhorst D, Maltusch A, Stockfleth E et al (2011) Reflectance confocal microscopy for the evaluation of acute epidermal wound healing. Wound Repair Regen 19(6):671–679. https://doi.org/10.1111/j.1524-475x.2011.00737.x
36. Wilkinson HN, Hardman MJ (2020) Wound healing: cellular mechanisms and pathological outcomes. Open Biol 10(9):200223. https://doi.org/10.1098/rsob.200223